Mon. Not. R. Astron. Soc. **365,** 813–826 (2006) doi:10.1111/j.1365-2966.2005.09748.x

On the role of strong gravity in polarization from scattering of light in relativistic flows

J. Horák[1,2] and V. Karas[1,2]★

[1]*Astronomical Institute, Academy of Sciences, Boční II, CZ-140 31 Prague, Czech Republic*
[2]*Charles University, Faculty of Mathematics and Physics, V Holešovičkách 2, CZ-180 00 Prague, Czech Republic*

Accepted 2005 October 15. Received 2005 October 15; in original form 2005 March 7

ABSTRACT

We study linear polarization due to scattering of light on a cloudlet of particles, taking into account the radiation drag and the gravitational pull exerted on them by a central body. The effects of special and general relativity are included by connecting a model of Beloborodov for the local polarization of scattered light with Abramowicz et al. formalism for the particle motion near an ultracompact star. The compactness of the central body and its luminosity are two critical parameters of the model. We discuss the polarization magnitude of photons, which are Thomson-scattered into direct and higher-order images. The importance of the latter is only moderate under typical conditions, but they may give rise to distinct features, which we explore in terms of a toy model. The scattered signal exhibits variations of intensity and of polarization with mutual time-lags depending on the beaming/focusing effects and the light traveltime.

Key words: black hole physics – polarization – relativity – scattering.

1 INTRODUCTION

Scattering of ambient light by fast moving flows has been recognized as a conceivable mechanism operating in different classes of objects. This process quite likely contributes to the linear polarization of initially unpolarized soft radiation upscattered in blazar jets (Begelman & Sikora 1987), winds from accretion discs (Beloborodov 1998) and in gamma-ray bursts (Shaviv & Dar 1995; Lazzati et al. 2004; Levinson & Eichler 2004). A significant level of intrinsic linear polarization of $\Pi \sim 3$ per cent was reported in a microquasar GRO J1655−40 (Scaltriti et al. 1997) and similarly for LS 5039 (Combi et al. 2004) in the optical band. A model of magnetized fireball polarization was discussed by Ghisellini & Lazzati (1999), who demonstrate that the expected polarization light curve should exhibit two peaks. Variations of the Galactic Centre linear polarization were reported in the millimeter band (Bower et al. 2005). Recently, Viironen & Poutanen (2004) brought attention to strong gravity effects in the polarimetry of accreting millisecond pulsars.

The idea of X-ray polarization studies providing clues to the physics of accreting compact objects was discussed in seminal papers (Angel 1969; Bonometto, Cazzola & Saggion 1970; Lightman & Shapiro 1975; Rees 1975; Sunyaev & Titarchuk 1985). Here we study a simple model with Thomson scattering on electrons ejected outwards from the centre or falling back; a novel point is that we consider strong gravity effects. The source of seed photons can be identified with the surface of a central star lying an arbitrary (finite) distance from the scatterer. Alternatively, it can represent an axially symmetric accretion disc near a black hole, a quasi-isotropic (ambient) radiation field, or a combination of all these possibilities. In order to avoid numerical complexities we do not discuss other radiation mechanisms that also produce polarization; that is, we do not consider the synchrotron self-Compton process, which is the most likely process wherever magnetic fields interact with relativistic particles (see Celotti & Matt 1994; Poutanen 1994 for discussion and for further references).

In the non-relativistic regime, a conceptually similar problem was examined by Rudy (1978) and Fox (1994), who considered the polarization of light of a finite-size star due to scattering on free electrons in a fully ionized circumstellar shell. These works showed that the non-negligible solid angle of the source subtended on the local sky of scattering particles has a depolarizing influence on the observed fractional polarization. This result was discussed by various authors, because the scattering of the stellar continuum is a probable source of net polarization of visible light in early-type stars, for which polarimetry has become a standard observational tool (e.g. Poeckert & Marlborough 1976; Brown & McLean 1977). General relativity effects are negligible in these objects; however, even the Newtonian limit is complex enough: the observed signal does not easily allow us to disentangle the contribution of a circumstellar shell, the primary radiation of the star and the effect of interstellar medium. In our case the situation becomes further complicated, because the system is highly time-dependent and mutual time delays along different light rays must be taken into account.

The general relativity signatures, which we discuss in this paper, reach maximum in a system containing a compact body with radius

★E-mail: vladimir.karas@cuni.cz

less than the photon circular orbit, i.e. $R_\star < r_{\rm ph}$. This can arise either as a result of a non-stationary system with $R_\star \equiv R_\star(t)$, presumably during a gravitational collapse, or it can represent a static ultracompact star if such exist in nature. Here we impose the spherical symmetry of the gravitational field, and so both situations are identical as far as the form of the space–time metric is concerned. The Schwarzschild vacuum solution describes the external gravitational field of all types of compact objects within general relativity, provided that their rotation is negligible and self-gravity of accreting matter does not contribute significantly to the gravitational field. We assume that these constraints are fulfilled. A sequence of $R_\star = {\rm const}$ situations can be employed in order to model a collapsing case.

The formalism that we apply works for a system with arbitrary compactness, even if the case of $R_\star = {\rm const} < r_{\rm ph}$ seems to be an unrealistically large compactness per se, likely violating the causality condition for neutron stars. Such a high compactness would thus be normally excluded; however, the situation has not yet been definitively settled (see Lattimer & Prakash 2004 for a recent review). According to astrophysically realistic equations of state, neutron star sizes do not reach ultracompact dimensions; their typical radii should exceed the photon circular orbit (Lattimer & Prakash 2001; Haensel 2003), and so the gravitational effects are constrained accordingly. However, the possibility of $R_\star$ being slightly less than $r_{\rm ph}$ persists, and there seems to be a growing awareness now of the fact that the very high density regime needs to be explored further.

Interest in ultracompact stars has been recently revived mainly in connection with gravitational waves in general relativity (Chandrasekhar & Ferrari 1991; Kokkotas, Ruoff & Andersson 2004). We can also consider more exotic options. Strange quark stars (e.g. Alcock, Farhi & Olinto 1986; Dey et al. 1998) can have their radii extending down to the Buchdal limit (see Weber 2005 for a recent review on other forms of quark matter and their relevance for compact stars). If nucleons can be confined at a density lower than nuclear matter density, then Q-stars could exist with a relatively high mass of $\sim 10^2\,{\rm M}_\odot$ and a radius as small as $R_\star \sim 0.9 r_{\rm ph}$ (e.g. Miller, Shahbaz & Nolan 1998). On a more speculative level is the idea of gravastars (Mazur & Mottola 2004), the compactness of which can exceed the Buchdal limit. Options for detecting the thermal radiation from different types of ultracompact stars have been recently discussed by McClintock, Narayan & Rybicki (2004). In the case of transiently accreting neutron stars, the crustal heating has been nominated as one of the relevant mechanisms generating thermal emission from the surface (Haensel & Zdunik 1990; Brown, Bildsten & Rutlege 1998).

The issue of realistic equations of state for ultracompact star matter is beyond the scope of the present paper, and likewise the actual observational information on masses and radii of compact stars (see, for example, Haensel 2003). It will be convenient to introduce a dimensionless parameter, $\zeta \equiv 1 - R_\star/r$, which maps the whole range of radii above the star surface on to the $\langle 0, 1\rangle$ interval, so that the form of graphs does not change with the star compactness. We consider the whole range of $0 \leqslant \zeta \leqslant 1$ allowed by general relativity. It is worth noticing that the formalism used below could also be readily applied to the case of an accretion disc as a source of light near a black hole. Obviously, a black hole represents a body with the maximum compactness and, at the same time, it is the most conservative option for such an ultracompact object (lower, axial symmetry of the disc radiation field limits the possibility of exploring the problem in an analytical way).

Our paper takes general relativity effects into account, including the effect of higher-order images if they arise. Although the signal is usually weak in these images, favourable geometrical arrangements are possible and, even more importantly, photons of the higher-order image experience a characteristic delay with respect to photons following a direct course. This delay (examined in detail by Bozza & Mancini 2004; Čadež & Kostić 2005) could help in revealing the presence of strong gravitational field in the system.

Our model provides a useful test bed for astrophysically more realistic schemes. In the next section we formulate the model and describe calculations. Then we show comparisons with previous results of other authors. We build our discussion on the approach of Beloborodov (1998, for polarization) and Abramowicz, Ellis & Lanza (1990, for the motion in combined gravitational and radiation fields in general relativity). In these papers the individual components of the whole picture were treated separately, while we connect them together in a consistent scheme. A reader interested only in the main results on polarization of higher-order images from light scattered on a moving cloudlet can proceed directly to Section 4.

As a final point of the introduction, it is worth noticing that Ghisellini, Haardt & Matt (2004) propose a model of aborted jets in which colliding clouds and shells occur very near a black hole and are embedded in a strong radiation field. According to their scheme, most energy dissipation should take place on the symmetry axis of an accretion disc. This would be another suitable geometry, in which a fraction of light is boosted in the direction of the photon circular orbit and eventually redirected to the observer. One may fear that the Thomson scattering approximation is not adequate to describe a turbulent medium in which electrons become very hot (Poutanen 1994); however, the accuracy should be still sufficient for energies of several keV, at which planned polarimeters are supposed to operate. Also, the seed photons have a different distribution when they originate from an accretion disc. However, we examined the variation of the polarization that an observer can expect from this kind of system (Horák 2005), and our calculations confirm that the expected polarization has a magnitude smaller but roughly similar to values predicted by the simple model adopted here.

2 MODEL AND CALCULATIONS

2.1 Set-up of the model and reference frames

We assume a fully ionized optically thin medium distributed outside the source of seed photons. These primary photons follow null geodesics until they are intercepted by an electron, which itself is moving under the mutual competition between gravity and radiation (we do not consider the effect of magnetic fields on the particle motion and radiation in this paper). Hence, we adopt the approximation of single scattering and we assume the Schwarzschild metric for the gravitational field of a compact body. We consider frequency-integrated quantities. The polarization vector of scattered light is propagated parallelly through the gravitational field to a distant observer and, in consequence, the polarization magnitude $\Pi(\boldsymbol{r}, \boldsymbol{n})$ and the redshifted intensity $\tilde{I} \equiv (1+\mathcal{Z})^{-4} I(\boldsymbol{r}, \boldsymbol{n})$ (expressed here in terms of the redshift $\mathcal{Z}$) are invariant.

The polarization is described in terms of Stokes parameters I, Q, U and V (Chandrasekhar 1960; Rybicki & Lightman 1979): I has the meaning of intensity along a light ray, Q and U characterize the linear polarization in two orthogonal directions (say $\boldsymbol{e}_X$ and $\boldsymbol{e}_Y$) in the plane perpendicular to the ray, and V is the circularity parameter. The polarization angle is defined by $\tan 2\chi = U/Q$. It gives the orientation of the major axis of the polarization ellipse with respect to $\boldsymbol{e}_X$. We can form a polarization basis in the local space by supplementing $\boldsymbol{e}_X$ and $\boldsymbol{e}_Y$ with another unit vector, $\boldsymbol{e}_Z$, pointed in the direction of the light ray. Three parameters are necessary to describe

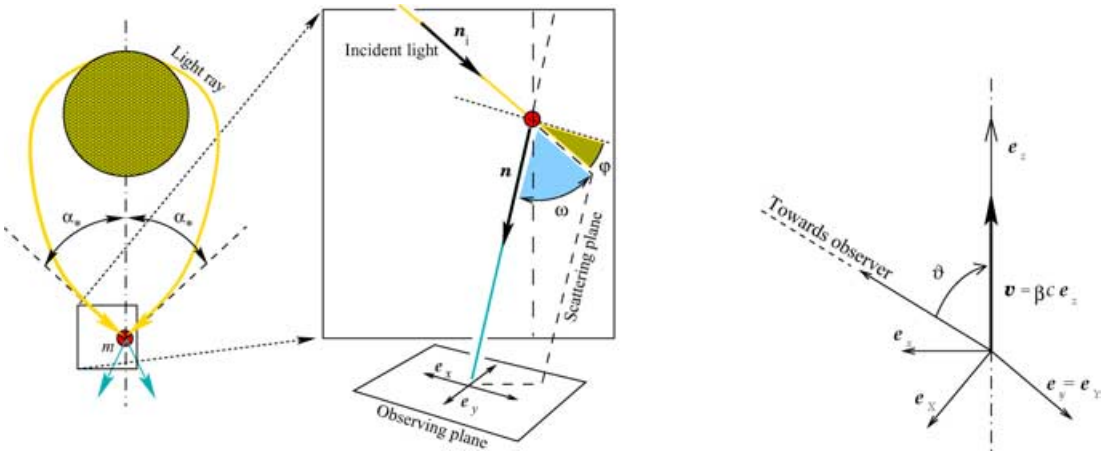

Figure 1. Geometry of the problem and the definition of angles.

a monochromatic beam, for which the condition $I^2 = Q^2 + U^2 + V^2$ holds. In the case of partially polarized light, the whole set of four parameters is generally required. It is then customary to define the degree of elliptical polarization, $\Pi \equiv I^{-1}(Q^2 + U^2 + V^2)^{1/2}$, which satisfies $0 \leqslant \Pi \leqslant 1$.

A four-dimensional tetrad can be constructed by extending the three base vectors and supplementing them with a purely time-like four-vector. A suitable choice of the tetrad is described below. Let us consider a simple case when the incident radiation field is axially symmetric in the laboratory frame (LF) with the basis ($\boldsymbol{e}_t$, $\boldsymbol{e}_x$, $\boldsymbol{e}_y$, $\boldsymbol{e}_z$).[1] Indices of four-vectors with respect to a local-frame basis are manipulated by the flat-space metric, diag $(-1, 1, 1, 1)$.

We orient $\boldsymbol{e}_z$ along the symmetry axis; the other two spatial vectors, $\boldsymbol{e}_x$ and $\boldsymbol{e}_y$, lie in a plane perpendicular to $\boldsymbol{e}_z$. Further, we assume that scattering electrons are streaming along the symmetry axis with four-velocity $\boldsymbol{u} = u^t \boldsymbol{e}_t + u^z \boldsymbol{e}_z$, where $u^t = c\gamma$ and $u^z = c\gamma\beta$ (γ is the Lorentz factor, and β is velocity in the LF divided by the speed of light). Later, we carry out a Lorentz boost to the comoving frame (CF) of the scatterer, ($\bar{\boldsymbol{e}}_t$, $\bar{\boldsymbol{e}}_x$, $\bar{\boldsymbol{e}}_y$, $\bar{\boldsymbol{e}}_z$), which is equipped with a time-like four-vector $\bar{\boldsymbol{e}}_t = \boldsymbol{u}$ and three space-like four-vectors $\bar{\boldsymbol{e}}_x = \boldsymbol{e}_x$, $\bar{\boldsymbol{e}}_y = \boldsymbol{e}_y$. The spatial part of $\bar{\boldsymbol{e}}_z$ is oriented in the direction of relative velocity of both frames.

Each incident photon of the ambient unpolarized radiation becomes highly polarized when scattered by a relativistically moving electron. The total polarization is eventually obtained by integrating over incident directions and the distribution of scattering electrons. In order to describe the propagation of scattered photons, we denote four-vectors $\boldsymbol{n} \equiv \boldsymbol{p}/p^t$ (with respect to the LF) and $\bar{\boldsymbol{n}} \equiv \boldsymbol{p}/\bar{p}^t$ (with respect to the CF), where $\boldsymbol{p}$ is the photon four-momentum (a null four-vector). Due to the axial symmetry we can assume $n^y = \bar{n}^y = 0$.

In addition to the above-defined reference frames, the LF and the CF, we introduce two 'polarization' frames: the laboratory polarization frame (LPF) with basis ($\boldsymbol{e}_t$, $\boldsymbol{e}_X$, $\boldsymbol{e}_Y$, $\boldsymbol{e}_Z$), and the comoving polarization frame (CPF) with the basis ($\bar{\boldsymbol{e}}_t$, $\bar{\boldsymbol{e}}_X$, $\bar{\boldsymbol{e}}_Y$, $\bar{\boldsymbol{e}}_Z$). The LPF is defined in such a way that $\boldsymbol{e}_Z$ is the three-space projection of the propagation four-vector $\boldsymbol{n}$, $\boldsymbol{e}_X$ lies in the $(\boldsymbol{e}_x, \boldsymbol{e}_z)$-plane, and $\boldsymbol{e}_Y$ is identical with the LF tetrad vector $\boldsymbol{e}_Y$. The CPF is defined analogically and indicated by bars over variables. Our definition of the reference frames is apparent from Fig. 1.

2.2 Stokes parameters in terms of the incident radiation stress-energy tensor

We start by calculating the polarization of the scattered radiation in the CPF. Conceptually, the model of local polarization is equivalent to that employed by Beloborodov (1998). The incident radiation is unpolarized with intensity $\bar{I}_\mathrm{i}$. It can be imagined as a superposition of two parallel beams of identical intensities, $\bar{I}_\mathrm{i}^{(1)} = \bar{I}_\mathrm{i}^{(2)} = \bar{I}_\mathrm{i}/2$, propagating along the $\bar{\boldsymbol{n}}_\mathrm{i}$ four-vector. The two beams are completely linearly polarized in mutually perpendicular directions and the scattered radiation is a mixture of both components. In the adopted choice of reference frames (see Fig. 1), the spatial projection of the propagation vector $\bar{\boldsymbol{n}}$ is identical to the spatial projection of $\bar{\boldsymbol{e}}_Z$. Unequal contributions $\bar{I}^{(1)}$ and $\bar{I}^{(2)}$ to the total intensity $\bar{I}$ result in net linear polarization of the scattered beam. According to this, $\bar{I}$, $\bar{Q}$ and $\bar{U}$ are non-zero, whereas the circularity parameter $\bar{V}$ vanishes.

Assuming that each scattered photon experiences one scattering event in an optically thin medium ($\tau \ll 1$), non-zero contributions to Stokes parameters are (Chandrasekhar 1960)

$$\delta\bar{I} = A\bar{I}_\mathrm{i}(1 + \cos^2\omega), \tag{1}$$

$$\delta\bar{Q} = -A\bar{I}_\mathrm{i}\,\cos 2\varphi\,\sin^2\omega, \tag{2}$$

$$\delta\bar{U} = -A\bar{I}_\mathrm{i}\,\sin 2\varphi\,\sin^2\omega, \tag{3}$$

where ω is the scattering angle between $\boldsymbol{n}_\mathrm{i}$ and $\boldsymbol{n}$, and $A \equiv 3\tau/(16\pi)$. The scattering takes place in the plane that forms an angle φ with the $\bar{x}$-axis. Angles φ and ω can be expressed using direction cosines, which are defined here as spatial components of the propagation four-vector $\bar{n}_\mathrm{i}$ of the incident beam, i.e. $\bar{n}_\mathrm{i}^X = \cos\varphi\,\sin\omega$, $\bar{n}_\mathrm{i}^Y = \sin\varphi\,\sin\omega$ and $\bar{n}_\mathrm{i}^Z = \cos\omega$. We obtain

$$\delta\bar{I} = A\left(1 + \bar{n}_\mathrm{i}^Z\bar{n}_\mathrm{i}^Z\right)\bar{I}_\mathrm{i}, \tag{4}$$

$$\delta\bar{Q} = A\left(\bar{n}_\mathrm{i}^Y\bar{n}_\mathrm{i}^Y - \bar{n}_\mathrm{i}^X\bar{n}_\mathrm{i}^X\right)\bar{I}_\mathrm{i}, \tag{5}$$

$$\delta\bar{U} = -2A\,\bar{n}_\mathrm{i}^X\bar{n}_\mathrm{i}^Y\bar{I}_\mathrm{i}. \tag{6}$$

[1] Hereafter we understand three-vectors as spatial projections of their corresponding four-vectors (and we do not introduce special notation for them; there is no danger of confusion). We stick to the conventional formalism of Stokes parameters, but we remark that it can be recast by employing a covariant definition of the polarization tensor, components of which are assembled using suitable combinations of Stokes parameters (Born & Wolf 1964). It has been argued (Portsmouth & Bertschinger 2005) that the latter approach may be found more elegant and useful for discussing the radiation transfer of polarized light through the medium in general relativity.

This form is useful, as it allows us to conveniently integrate the partial contributions over incident directions to obtain

$$\bar{I} = Ac(\bar{T}^{tt} + \bar{T}^{ZZ}), \tag{7}$$

$$\bar{Q} = Ac(\bar{T}^{YY} - \bar{T}^{XX}), \tag{8}$$

$$\bar{U} = -2Ac\bar{T}^{XY}, \tag{9}$$

for the total Stokes parameters of scattered light. We denote

$$\bar{T}^{\mu\nu} \equiv \frac{1}{c}\int_{4\pi} \bar{n}_{\rm i}^{\mu}\bar{n}_{\rm i}^{\nu}\bar{I}_{\rm i}(\bar{\boldsymbol{n}}_{\rm i})\,{\rm d}\Omega \tag{10}$$

the stress-energy tensor of the incident radiation field.

We remind that the incident radiation was assumed axially symmetric in the CF; therefore, the only non-zero components in this frame are $\bar{T}^{tt}$, $\bar{T}^{tz}$, $\bar{T}^{zz}$, $\bar{T}^{xx}$ and $\bar{T}^{yy}$. These are further constrained by symmetry: $\bar{T}^{xx} = \bar{T}^{yy} = (\bar{T}^{tt} - \bar{T}^{zz})/2$. A relation to the CPF components can be obtained by rotation about the $\bar{y}$-axis by angle $\bar{\vartheta}$. Using equations (7)–(9) we find

$$\bar{I} = \frac{1}{2}Ac[(3\bar{T}^{tt} - \bar{T}^{zz}) - (\bar{T}^{tt} - 3\bar{T}^{zz})\cos^2\bar{\vartheta}], \tag{11}$$

$$\bar{Q} = \frac{1}{2}Ac(\bar{T}^{tt} - 3\bar{T}^{zz})\sin^2\bar{\vartheta}. \tag{12}$$

The Stokes parameter $\bar{U}$ vanishes due to axial symmetry. The scattered radiation is partially polarized either in the $(\bar{x},\bar{z})$-plane, or perpendicularly to it. The former and the latter cases will be referred to as longitudinal and transverse polarization, respectively. Later, in Section 3, we demonstrate that this change can occur also with a group of cold electrons, whose bulk motion is determined by the radiation and gravitational fields of a star and recorded in the LF.

The degree of polarization is calculated directly from the definition

$$\Pi(\bar{\vartheta}) = \frac{|\bar{Q}|}{\bar{I}} = \frac{|\Pi_{\rm m}|\sin^2\bar{\vartheta}}{1 - \Pi_{\rm m}\cos^2\bar{\vartheta}}\,, \tag{13}$$

where

$$\Pi_{\rm m} \equiv \frac{\bar{T}^{tt} - 3\bar{T}^{zz}}{3\bar{T}^{tt} - \bar{T}^{zz}}. \tag{14}$$

This result is equivalent to equations (4) and (5) in Beloborodov (1998), who applied the model of Thomson scattering to winds outflowing from a plane-parallel disc slab. Beloborodov also calculated the polarization of scattered radiation and found that its sign depends on the wind velocity. In our notation the change is captured in $\Pi_{\rm m}$, which acquires values in the range $-1 \leqslant \Pi_{\rm m} \leqslant 1$. Its meaning is evident from equation (13): the absolute value $|\Pi_{\rm m}|$ is the maximum degree of polarization of the scattered light and the sign of $\Pi_{\rm m}$ determines the sign of the $\bar{Q}$-parameter.

In order to determine the polarization magnitude as seen by an observer in the LF, we carry out the Lorentz boost (e.g. Cocke & Holm 1972; Rybicki & Lightman 1979). The angle of observation $\bar{\vartheta}$ is transformed according to

$$\sin\bar{\vartheta} = \mathcal{D}\,\sin\vartheta, \qquad \cos\bar{\vartheta} = \gamma\mathcal{D}\,(\cos\vartheta - \beta), \tag{15}$$

where $\mathcal{D} \equiv \gamma^{-1}(1 - \beta\cos\vartheta)^{-1}$ is the Doppler factor. The Stokes parameters are transformed in the same manner as the radiation intensity and the boost retains the four-vector $\boldsymbol{e}_y$ unchanged: $I = \mathcal{D}^4\bar{I}$ and $Q = \mathcal{D}^4\bar{Q}$. It follows that the polarization magnitude $|\Pi_{\rm m}|$ is Lorentz-invariant. By transforming all relevant quantities to the LF, we obtain Stokes parameters of scattered radiation:

$$\begin{aligned} Q &= \frac{1}{2}Ac\mathcal{D}^6\gamma^2 \\ &\quad\times[(1-3\beta^2)T^{tt} + 4\beta T^{tz} - (3-\beta^2)T^{zz}]\sin^2\vartheta, \\ I &= Ac\mathcal{D}^4\gamma^2\left[(1+\beta^2)(T^{tt}+T^{zz}) - 4\beta T^{tz}\right] + Q. \end{aligned} \tag{16}$$

2.3 Critical velocities

The aim of this subsection is to connect, in a self-consistent manner, the properties of particle motion through the ambient radiation field with Stokes parameters of scattered light. In order to prepare for this discussion, it is useful to introduce two critical velocities of the particle motion.

First, of particular interest is the velocity at which the polarization of scattered radiation vanishes (Beloborodov 1998). The condition for velocity follows from the requirement

$$\bar{T}^{tt} - 3\bar{T}^{zz} = 0. \tag{17}$$

Performing the Lorentz boost to the LF, we obtain

$$(1-3\beta^2)T^{tt} + 4\beta T^{tz} + (\beta^2 - 3)T^{zz} = 0. \tag{18}$$

This is a quadratic equation for β, which has two roots

$$\beta_{1,2} = a \pm \sqrt{a^2 + b}, \tag{19}$$

where

$$a \equiv \frac{2T^{tz}}{3T^{tt} - T^{zz}}, \qquad b \equiv \frac{T^{tt} - 3T^{zz}}{3T^{tt} - T^{zz}}. \tag{20}$$

Clearly, equation (18) can be satisfied independently of the direction of observation. For $\beta \to \beta_{1,2}$ the polarization changes from longitudinal to transversal.

Secondly, we introduce the saturation velocity β_0 (Sikora & Wilson 1981). As was shown by various authors under different approximations about the particle cross-section and the form of gravitational field (see, for example, Melia & Königl 1989; Abramowicz et al. 1990; Vokrouhlický & Karas 1991; Fukue & Hachiya 1999; Keane, Barrett & Simmons 2001), the saturation velocity plays an important role in the dynamics of relativistic jets: particles moving at velocity smaller/greater than the saturation velocity gain/lose their momentum at the expense of the radiation field. In the absence of other acceleration mechanisms and neglecting the inertia of particles, the effect of radiation pressure eventually leads to $\beta \to \beta_0$ as the terminal speed of the particle motion.

The saturation velocity is determined by the requirement of the vanishing radiation flux in the CF, i.e.

$$\bar{T}^{tz} = 0. \tag{21}$$

This gives another quadratic equation

$$(1+\beta^2)T^{tz} - \beta(T^{tt} + T^{zz}) = 0, \tag{22}$$

with the solution

$$\beta_0 = \frac{1 - \sqrt{1-\sigma^2}}{\sigma}, \tag{23}$$

where $\sigma \equiv 2T^{tz}/(T^{tt} + T^{tz})$. We ignore the second solution, as it has no physical meaning.

As an example let us assume the incident radiation field to be strictly isotropic in the laboratory frame, i.e.

$$T^{\alpha\beta} = {\rm diag}\left(\mathcal{E}, \frac{1}{3}\mathcal{E}, \frac{1}{3}\mathcal{E}, \frac{1}{3}\mathcal{E}\right) \tag{24}$$

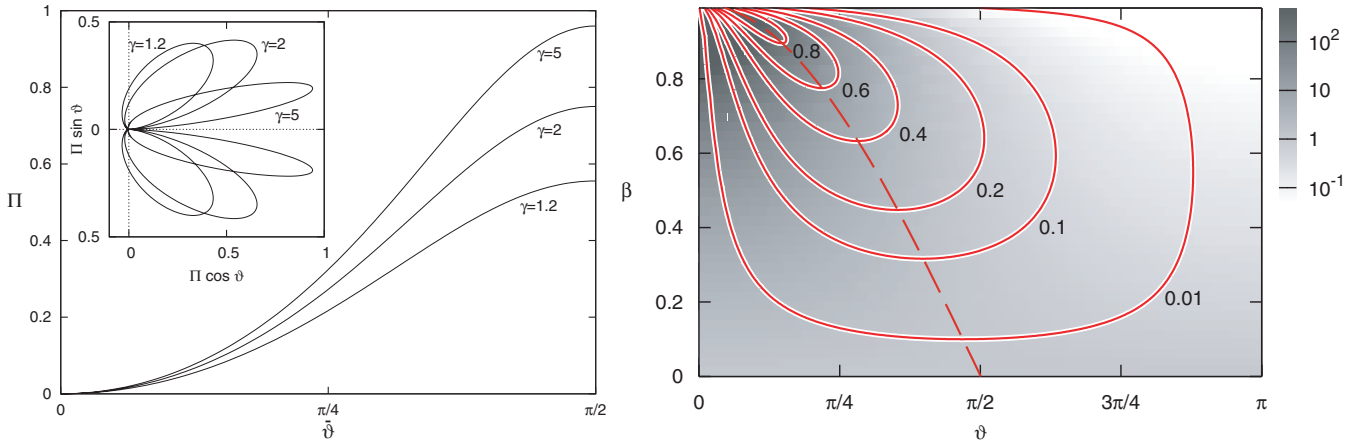

Figure 2. Left: the magnitude of transversal polarization $\Pi(\bar{\vartheta};\gamma)$ due to upscattering by a relativistic electron as a function of observing angle in the local comoving frame. The case of the locally isotropic ambient radiation field is shown for three different values of the Lorentz factor γ. In the inset, the emission diagram shows the corresponding LF polarization. The lobes become gradually flattened toward the front direction of motion as γ increases. We can see from equation (11) that the graph of $\Pi(\bar{\vartheta})$ is symmetrical with respect to $\bar{\vartheta} = \pi/2$. This corresponds to a well-known fact that polarization is maximum for the radiation scattered perpendicularly to the axis of symmetry in the CF. Right: contours of $\Pi(\vartheta, \beta)$ are shown superposed on the density plot of $I(\vartheta, \beta)$. Levels of shading give the intensity (in arbitrary units) and illustrate the progressive beaming towards the $\vartheta = 0$ direction in the ultrarelativistic limit (in the LF). On the other hand, given a value of β, the polarization degree $\Pi(\vartheta;\beta)$ as a function of ϑ reaches maximum at a non-zero angle, always off-axis (dashed line).

with $\mathcal{E} \equiv T^{tt}$ being the energy density of radiation. Evaluating the stress-energy tensor in the CF we find $\Pi_{\rm m} = -\beta^2$. Substituting into equation (13) we obtain the polarization degree

$$\Pi(\bar{\vartheta}, \beta) = \frac{\beta^2 \sin^2 \bar{\vartheta}}{1 + \beta^2 \cos^2 \bar{\vartheta}}. \tag{25}$$

Lorentz transformation to the LF gives

$$\Pi(\vartheta, \beta) = \frac{\beta^2 \sin^2 \vartheta}{(2\gamma^2 - 1)\,(1 - \beta \cos \vartheta)^2 - \beta^2 \sin^2 \vartheta}. \tag{26}$$

Because $\Pi_{\rm m} \leqslant 0$, the scattered radiation is polarized transversely. The critical velocities are $\beta_0 = \beta_1 = \beta_2 = 0$ in this case.

Fig. 2 shows the dependence of Π on observing angle according to equation (26). It is worth noticing that we explore the frequency-integrated model, because this assumption is adequate for the purpose of clarification of the role gravitational lensing (discussed in the next section). The same dependency of Stokes parameters on the scatterer velocity and observer viewing angle is obtained in the frequency-dependent calculation with the spectral index of the incident radiation equal to -1 (the case adopted originally by Begelman & Sikora 1987). Our results are consistent with Lazzati et al. (2004) provided that appropriate averaging over energy is adopted. It can be seen (in the left panel of Fig. 2) that the resulting curves closely resemble the numerical result of (Lazzati et al. 2004, see their fig. 1). In particular, the curves are identical for $\gamma \gg 1$ and they approach the ultrarelativistic limit $\Pi = (1 - \cos^2 \bar{\vartheta})/(1 + \cos^2 \bar{\vartheta})$ (originally examined again by Begelman & Sikora 1987, and invoked more recently, for example, by Shaviv & Dar 1995). This limit corresponds to the case of a head-on collision, when all photons are impinging at incident angles $\bar{\vartheta}_{\rm i} \to \pi$ because of aberration in the CF.

For moderate Lorentz factors there is some difference between our profile of $\Pi(\bar{\vartheta})$ and the corresponding numerical values plotted in Lazzati et al. (2004). For example, checking the $\gamma = 2$ curve, we notice that the relative difference amounts to roughly 13 per cent. This apparent discrepancy is explained by realizing that our equation (26) has been derived in terms of bolometric intensities, whereas Lazzati et al. employ specific (frequency-dependent) quantities. By integrating their Stokes parameters over frequency we recover precisely the value predicted by equation (26). See Horák (2005) for detailed comparisons.

3 POLARIZATION OF LIGHT SCATTERED NEAR A COMPACT STAR

3.1 Gravitational and radiation fields

The gravitational field of a spherically symmetric star is described by the Schwarzschild metric (Chandrasekhar 1992)

$$\mathrm{d}s^2 = -c^2 \xi\, \mathrm{d}t^2 + \xi^{-1}\, \mathrm{d}r^2 + r^2\, \mathrm{d}\Omega^2, \tag{27}$$

where $\mathrm{d}\Omega$ is the angular part of a spherically symmetric line element, $\xi(r) \equiv 1 - R_{\rm S}/r$ is the redshift function in terms of the Schwarzschild radius, $R_{\rm S} \equiv 2GMc^{-2} \doteq 2.95 \times 10^5 (M/{\rm M}_\odot)$ cm, and M is the mass of the star. Four-vectors and four-tensors are expressed with respect to a local orthonormal tetrad, $[\boldsymbol{e}^{(t)}, \boldsymbol{e}^{(r)}, \boldsymbol{e}^{(\theta)}, \boldsymbol{e}^{(\phi)}]$, with non-vanishing components $e_t^{(t)} = c\xi^{1/2}, e_r^{(r)} = \xi^{-1/2}, e_\theta^{(\theta)} = r$ and $e_\phi^{(\phi)} = r\,\sin\theta$. Tetrad components of four-vectors are denoted by bracketed indices and are raised and lowered using the Minkowski metric.

Primary photons are emitted from a star and form the ambient radiation field acting on the particle. The star of radius $R_\star$ and compactness $R_\star/R_{\rm S}$ appears to a static observer, located at radius r, as a bright disc of angular radius $\alpha_\star = \alpha(r)$

$$\sin \alpha(r) = \frac{\tilde{R}}{r}\, \frac{\xi(r)^{1/2}}{\xi(\tilde{R})^{1/2}}, \tag{28}$$

where $\tilde{R} \equiv \max\{(3/2)R_{\rm S}, R_\star\}$. Because of light bending, the solid angle subtended by a compact star on the sky is larger than the Euclidean (flat space) estimate. Equation (29) was originally discussed by Synge (1967) and the manifestation of the gravitational self-lens effect was examined by Winterberg & Phillips (1973).

In the case of very high compactness (when $R_\star < (3/2)R_{\rm S}$) the rim of the image is formed by photons encircling the perimeter of the star more than once. In spite of complicated trajectories of photons, to the observer the surface appears radiating with intensity

(we neglect limb darkening for simplicity)

$$I(r) = \frac{\xi(R_\star)^2}{\xi(r)^2}\, I_\star(R_\star). \tag{29}$$

Let us take the previous example from equation (25), but assume that the source of primary photons occupies only a fraction of the local sky of the scattering particle. Gradual dilution of the source radiation with distance is described by function $\alpha(r)$. The limit of $\alpha \to \pi$ corresponds to strictly isotropic radiation arriving from all directions, whereas for $\alpha \to 0$ we obtain the case of a point-like source. We thus recognize the results of Section 2.3.

The stress-energy tensor of the stellar radiation field has three independent components: the energy density, the energy flux and the radial stress. These are given, respectively, by

$$\mathcal{E}_\star \equiv T_\star^{(t)(t)} = \frac{2\pi}{c} I\,(1-\cos\alpha)\,, \tag{30}$$

$$\mathcal{F}_\star \equiv cT_\star^{(t)(r)} = \pi I \sin^2\alpha, \tag{31}$$

$$\mathcal{P}_\star \equiv T_\star^{(r)(r)} = \frac{2\pi}{3c} I(1-\cos^3\alpha). \tag{32}$$

There are two other non-zero components, $T_\star^{(\theta)(\theta)} = T_\star^{(\phi)(\phi)}$, which can be computed from the condition $T_{\star\sigma}^{\sigma} = 0$. The magnitude of the star radiation is characterized by total luminosity, $L_\star = 4\pi R_\star^2 \mathcal{F}_\star(R_\star)$.

Finally, we include another, isotropic component of the radiation field with intensity $I_{\rm iso}$ in addition to stellar light. The corresponding stress-energy tensor is entirely determined by energy density $\mathcal{E}_{\rm iso} = 4\pi c^{-1} I_{\rm iso}$. The stress-energy tensor of the total radiation field is the sum $T^{\alpha\beta} = T_\star^{\alpha\beta} + T_{\rm iso}^{\alpha\beta}$. Combining the two contributions allows us to model different situations according to their relative magnitude and the motion of the scattering medium.

3.2 Polarization of scattered light

We first assume velocity of the scatterer $\beta(r)$ and compute the resulting polarization. Fig. 3 shows the effect of vanishing and changing polarization, which occurs at a particular value of β. We compare two situations: the case of the purely stellar component of the primary irradiation, as described in Section 2 (in the left panel of Fig. 2), versus the case of a sum of the isotropic component and radiation coming from the star surface (on the right). The latter configuration represents an anisotropic irradiation of an electron; it can be parametrized by the mutual ratio of redshifted radiation intensities received at a distant observer, i.e.

$$\lambda_{\rm i} \equiv \frac{\tilde{I}_{\rm iso}}{\tilde{I}_\star}. \tag{33}$$

This can be considered as a toy model of inverse Compton upscatter in an illuminated jet where the intensity of ambient light is not directly connected with the intensity of the central source. $\lambda_{\rm i} =$ const is a free parameter of the model; given a value, the degree of anisotropy depends on the distance from the star in $R_{\rm S}$. It is worth noticing that light bending is taken into account in this calculation automatically, including all higher-order images encircling the star.

Polarization is non-zero provided that particle velocity is not equal to $\beta_{1,2}(r)$ and, indeed, Π can reach large values. This is shown in Fig. 4, where we plot the extremal value of function $\Pi_{\rm m}(\beta, \zeta)$ in the plane of particle velocity versus distance. $|\Pi_{\rm m}(\beta, \zeta)|$ is equal to extremes of the polarization degree measured along a suitably chosen observing angle ϑ. The curve of zero polarization is also plotted and we notice that it is independent of ϑ. In this figure the primary unpolarized light was assumed to be a mixture of stellar and ambient contributions (the latter component was assumed to be distributed isotropically in the LF). The saturation curve $\beta_0(\zeta)$ is shown and it is worth noticing that, for some values of the model parameters, $\beta_0(\zeta)$ crosses the contour of $\Pi = 0$. Therefore, a hypothetical particle moving or oscillating along the saturation curve would exhibit polarization that swings its direction by right angle.

We can modify the previous example by considering a constant ratio of energy density, i.e. by replacing $\lambda_{\rm i}$ with another parameter

$$\lambda_{\rm e} \equiv \frac{\mathcal{E}_{\rm iso}}{\mathcal{E}_\star(r)}. \tag{34}$$

This definition captures better the case when the ambient light originates from scattering of the central component (perhaps on clumps being accreted on to the star), so that both contributions are linked to each other and their energy density decreases at an identical rate with the distance. We again constructed graphs of $\Pi_{\rm m}(\beta, \zeta)$ and found

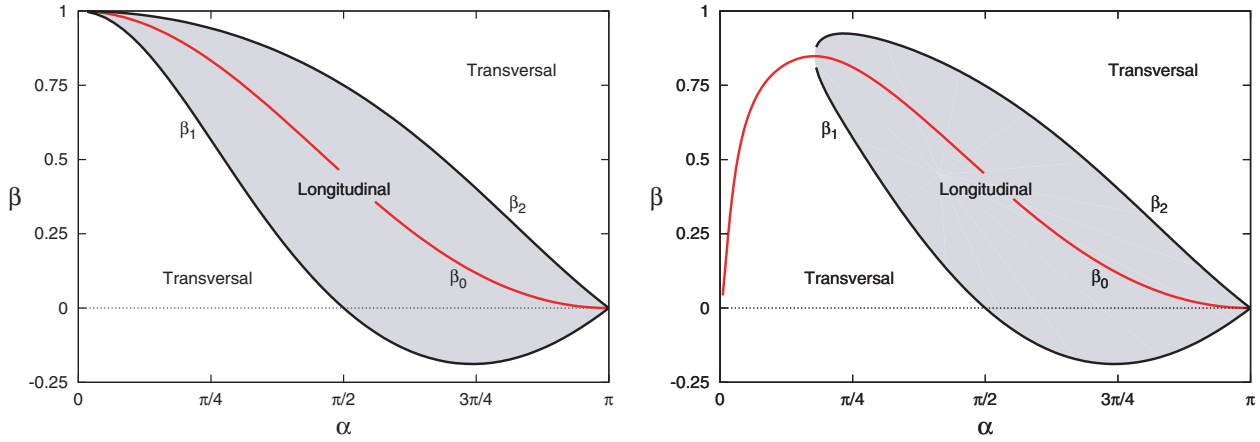

Figure 3. Left: the case of incident radiation originating from an isotropic source of angular radius α (see equations 31–33). Two branches of critical velocity are shown, $\beta_1(\alpha)$ and $\beta_2(\alpha)$, at which the total polarization of scattered light vanishes independent of observing direction. The saturation curve $\beta_0(\alpha)$ is also plotted assuming that the radiation drag dominates the particle dynamics. Right: the same as on the left but for a mixture of two components of the incident radiation, i.e. the ambient isotropic ($\alpha = \pi$) source plus the stellar (non-isotropic) contribution according to equation (34) with $\lambda_{\rm i} = 0.001$. In both panels, the regions of longitudinal and transversal polarization are distinguished by shading.

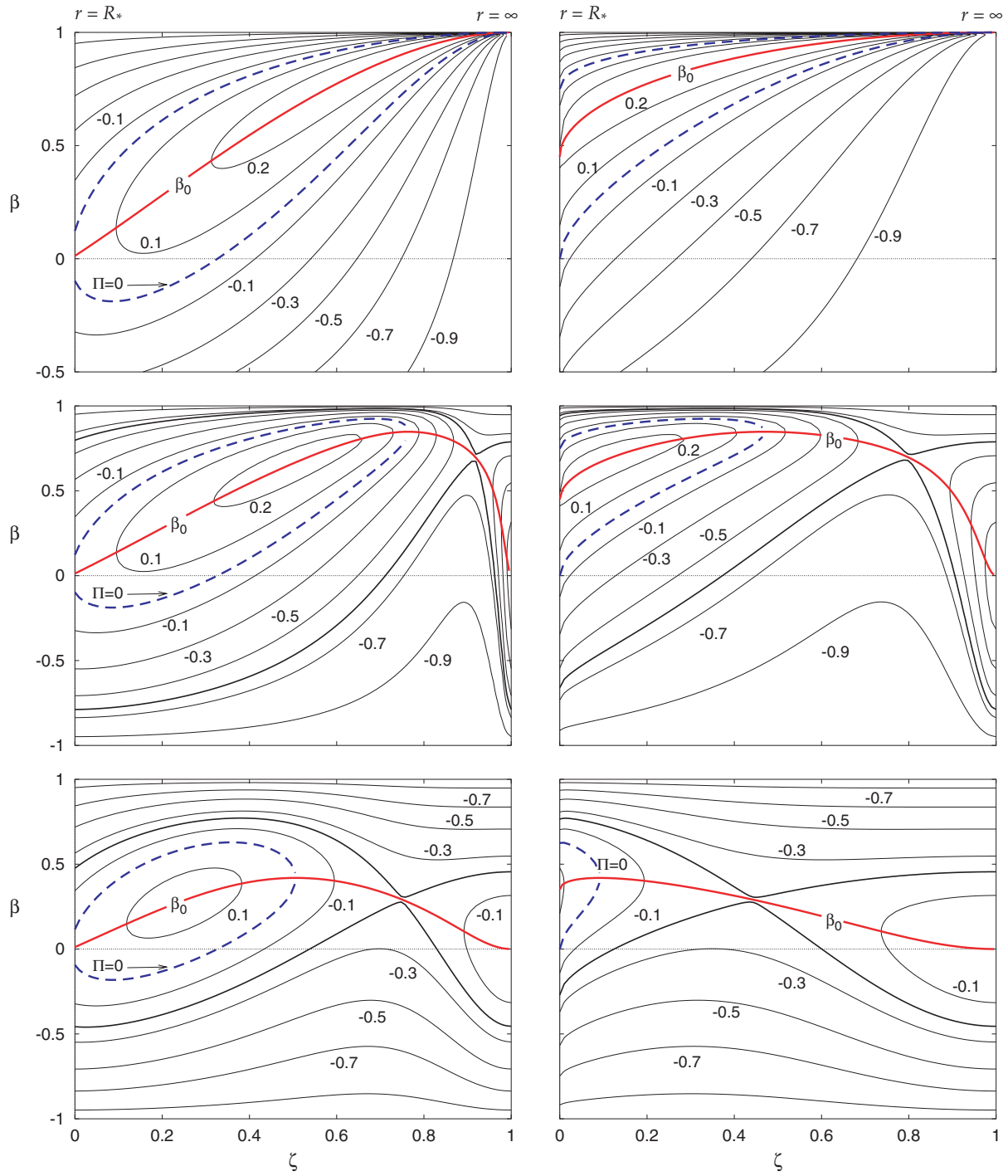

Figure 4. Contours of extremal values of the polarization function $\Pi_{\rm m}(\beta, \zeta)$ for photons Thomson-scattered on an electron, moving with a given velocity β through a mixture of stellar and ambient diffuse light. Each panel captures the whole range of radii from $r = R_\star$ ($\zeta = 0$) to $r \to \infty$ ($\zeta = 1$). The three rows correspond to progressively increasing luminosity parameter (34): (i) $\lambda_{\rm i} = 0$ (top); (ii) $\lambda_{\rm i} = 0.001$ (middle); (iii) $\lambda_{\rm i} = 0.1$ (bottom). The left column is for a highly compact star with $R_\star = 1.01 R_{\rm S}$; the right column is for $R_\star = 10^3 R_{\rm S}$. Hence, the light-bending effects are significant on the left and negligible on the right. The curve of zero polarization $\Pi = 0$ is plotted with a dashed line. Generally, if the star is sufficiently compact, then the curve of zero polarization becomes double-valued; its two branches correspond to $\beta \equiv \beta_{1,2}(\zeta)$ in Fig. 3. A separatrix is a particular contour that distinguishes regions of different topology in this graph. The saturation curve $\beta_0\,(\zeta)$ is also plotted.

a similar structure of contours at small radii such as those shown in Fig. 4, including the double-valued function $\beta_{1,2}(\zeta)$. However, the saturation velocity $\beta_0(\zeta)$ does not fall to zero at $r \to \infty$; instead, it generally reaches substantially higher values. Moreover, the critical point (where the separatrix curve self-crosses) is lost, as well as the whole structure towards the right of the critical point.

Polarization of scattered light obviously depends on scatterer motion and these can be calculated consistently. In the next section

we finally determine velocity $\beta(r)$ along the particle trajectories, for which the luminosity of the star and its compactness are parameters.

3.3 Polarization along the particle trajectory

The four-velocity $\boldsymbol{u}$ of a particle can be found by solving the equation of motion in the form (Abramowicz et al. 1990)

$$mu_\rho \nabla^\rho u^\alpha = -\frac{\sigma_\mathrm{T}}{c} h^\alpha_\rho T^{\rho\sigma} u_\sigma, \tag{35}$$

where m is the particle rest mass and $h^\nu_\mu \equiv \delta^\nu_\mu + c^{-2}u^\nu u_\mu$ is a projection tensor. The left-hand side of equation (36) includes the effect of gravity (∇ denotes covariant differentiation with respect to curved space–time geometry) and the right-hand side provides the effect of radiation drag – accelerating or decelerating particles with respect to free-fall motion.

The non-zero components of four-velocity are $u^{(t)} = c\gamma$ and $u^{(r)} = c\gamma\beta$ in the local tetrad of a static observer.[2] Equation (36) takes the form

$$\dot{\beta} = \frac{1}{c\gamma^2}\left[\frac{\xi^{1/2}}{\gamma^2}\frac{F^{(r)}_\mathrm{rad}}{m} - \frac{c^2 R_\mathrm{S}}{2r^2}\right], \tag{36}$$

$$\dot{r} = c\xi\beta, \tag{37}$$

where the dot denotes derivative with respect to coordinate time t and $F^{(r)}_\mathrm{rad}$ is the radial component of the radiation force

$$F^{(r)}_\mathrm{rad} = \sigma_\mathrm{T}\gamma^3\left\{(1+\beta^2)T^{(t)(r)} - \beta\left[T^{(t)(t)} + T^{(r)(r)}\right]\right\}. \tag{38}$$

The effect of radiation on the motion is expressed by the first term in the parentheses on the right-hand side of equation (37), whereas the other term can be considered as the contribution of gravity. Hence, the particle dynamics depends on the relative strength of the radiation and gravitational fields. Because of the redshift factor near a compact star these two influences do not obey the same simple Newtonian law, and so a rich set of possible results emerges. These can be parametrized by Eddington luminosity L_E, which follows from the condition of zero acceleration for matter hovering at radius $r = R_\star$. The radiation force becomes $F^{(r)}_\mathrm{rad} = (\sigma_\mathrm{T} L_\star)/(4\pi R_\star^2 c)$ and equation (37) with $\dot{\beta} = 0$ gives

$$L_\mathrm{E} = \frac{2\pi m c^3 R_\mathrm{S}}{\sigma_\mathrm{T}\xi(R_\star)^{1/2}}. \tag{39}$$

We note that the acceleration depends on the radial distance from the centre as well as on particle velocity. The relative importance of radiation and gravity is characterized by the dimensionless factor

$$\Gamma \equiv \frac{L_\star}{L_\mathrm{E}}. \tag{40}$$

The radiation term in acceleration is regulated by the interplay of relativistic aberration and the Doppler boosting, which tend to establish the saturation velocity. At this point further acceleration vanishes, i.e. $\dot{\beta}_0(r) = 0$. Considering only radiation from the star and expressing the explicit form of the stress-energy tensor, equations (37) and (38) reduce to equation (2.3) of Abramowicz et al. (1990). With gravitational attraction of the centre taken into account, the possibility occurs of an equilibrium point $\zeta_\mathrm{eq} \equiv \zeta(r = R_\mathrm{eq})$, where a particle can reside. By setting $\beta = 0$ and $\dot{\beta} = 0$ in equations (37)–(39), we can find that the equilibrium radius ranges from $R_\mathrm{eq}(\Gamma) \to R_\star$ (i.e. $\zeta_\mathrm{eq} \to 0$) for $\Gamma \to 1$ up to $R_\mathrm{eq}(\Gamma) \to \infty$ (i.e. $\zeta_\mathrm{eq} \to 1$) for $\Gamma \to \sqrt{3}$.

Equations (37)–(38) allow for a finite set of topologically different solutions. These can be classified into different categories (Abramowicz et al. 1990; see also Keane et al. 2001) according to the behaviour of saturation curves in the (β, ζ)-plane. Notice that we have already examined one of these solutions, i.e. the saturation curve (24) for very high luminosity of the star and negligible mass of the particle, i.e. $\Gamma \to \infty$. The motion is then governed solely by radiation drag. We select this condition because it is particularly relevant for the discussion of the resulting polarization of scattered light. Its role can be inferred also from Fig. 4, where the β_0-curve for this case passes through the critical point of contour lines of $\Pi(\beta, \zeta)$. The limit of $\Gamma \to \infty$ is an extreme case. The different profile $\beta_0(\zeta)$ applies to moderate values of the luminosity parameter, $\Gamma < \infty$, when particles do not strictly maintain the saturation velocity because of inertial effects acting on them.

Different categories of the particle motion then provide a natural framework also for the discussion of the resulting polarization. The three most important cases are recorded in Fig. 5. In this example only the stellar radiation is taken into account, whereas the component $I_\mathrm{iso} = 0$ for simplicity. The cases shown here correspond to the situation when (i) the radiation field dominates over gravity and the electron is therefore pushed away to an infinite radius (see the left panel), (ii) a moderate value of the luminosity allows the scattering electrons to reach an equilibrium position at $\zeta \equiv \zeta_\mathrm{eq} = 0.62$ (middle), and (iii) the luminosity is very small and the particles are almost free-falling in the gravitational field (right). Particles start from $\zeta = 0$ and they quickly adhere to the saturation curve $\beta_0(\zeta;\Gamma)$, provided that radiation is dynamically important, i.e. in cases (i) and (ii). This occurs independently of initial velocity; then, the motion follows a curve adjacent to but slightly different from the saturation curve. On the other hand, in case (iii) the gravitation governs the motion; the trajectory $\beta(\zeta)$ is only slightly asymmetric with respect to the $\beta = 0$ line by the weak influence of radiation.

By coupling the equations of particle motion with the polarization equations of Section 3.2 we obtain Stokes parameters of scattered light along each particle trajectory. The bottom panels of Fig. 5 show the resulting magnitude of polarization. Notice how it crosses zero level at a certain distance of the scatterer from the stellar surface. At this point, polarization changes direction from transverse to longitudinal. The points of intersection of curves $\beta_{1,2}(\zeta)$ with the particle motion $\beta(\zeta)$ determine the radial location of the point of vanishing polarization (indicated by dotted vertical lines in the plot).

We now assume that a small cloudlet is formed by a group of electrons. We can distinguish three cases, depending on the bulk velocity of the cloudlet. These are discussed in Sections 4.1–4.3. The predicted time dependence offers a way to test the model.

4 POLARIZATION FROM A CLOUDLET

4.1 The case of fast ejection ($\gamma \gg 1$)

Let us denote $R_\mathrm{cl} \ll R_\mathrm{S}$ the radius of the cloud and $\psi \sim R_\mathrm{cl}/z$ its angular radius as seen from the centre. We assume that the cloud has

[2] In this paper we consider purely radial motion. The same formalism can be readily applied to more complicated motion of the scatterer, although it will then hardly be possible to solve both the motion and the resulting polarization analytically. Notice that the case of clumps orbiting in the plane of a black hole accretion disc was discussed by Pineault (1977), Connors, Stark & Piran (1980) and Bao et al. (1997). These authors also pointed out that effects of general relativity could be discovered by tracing time variable polarization.

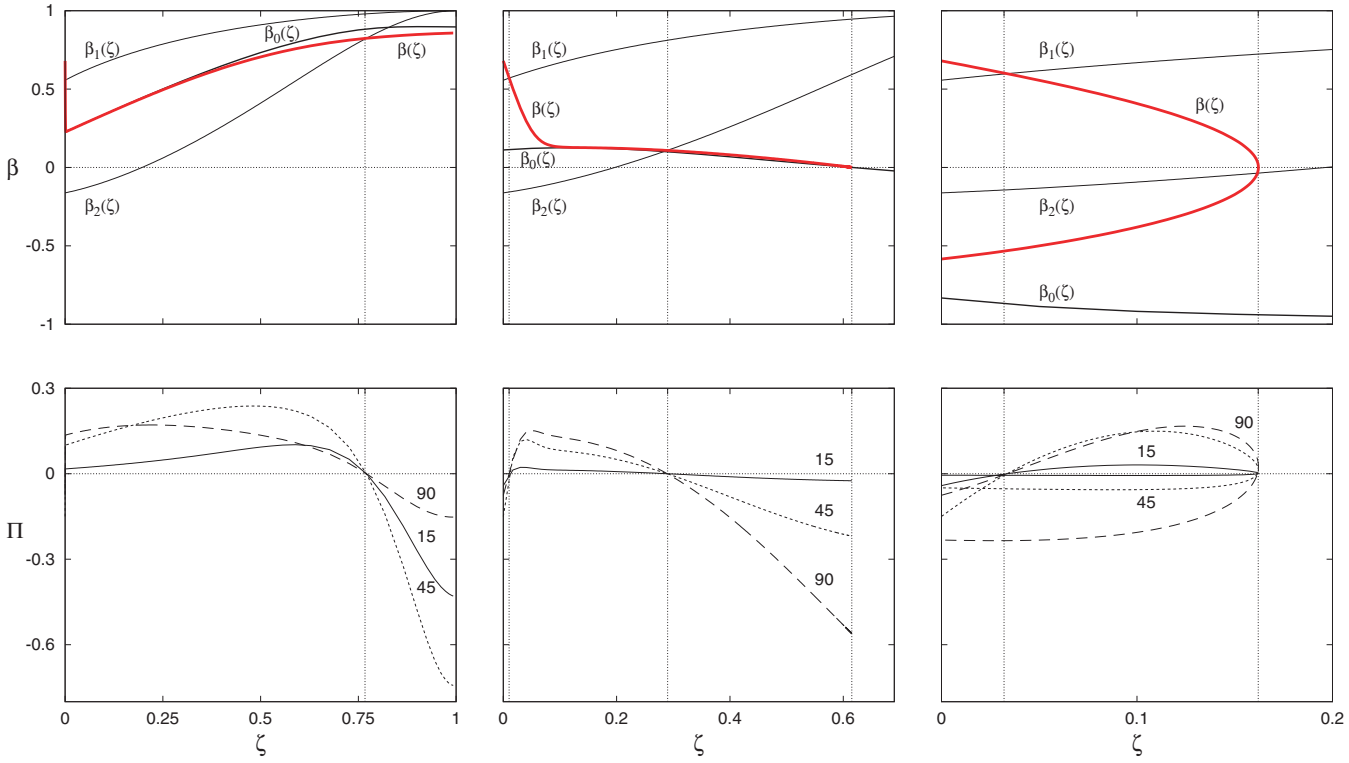

Figure 5. Top row: particle velocity $\beta(\zeta)$ (thick curve) and the three critical velocities β_0, β_1 and β_2 in the combined radiation and gravitational fields. Each trajectory starts from the star, $R_\star = 1.205 R_S$ ($\zeta = 0$), and it proceeds towards infinity ($\zeta = 1$). Positive values of β correspond to an outflow; negative values are for an inflowing material. Three cases are shown for different values of dimensionless luminosity: $\Gamma = 100$ (left), $\Gamma = 2$ (middle) and $\Gamma = 0.1$ (right). Bottom row: the polarization magnitude $\Pi(\zeta)$ along the particle trajectories corresponding to the three solutions given above. In each panel, the curves are labelled with the observing angle ϑ. All curves have a common zero-point where they cross each other. The sign of Π distinguishes here the case of transversal polarization from longitudinal polarization.

small optical depth, $\tau_{\rm cl} \ll 1$, and it is ejected along the z-axis, with bulk velocity $\beta(z) \gg 0$ directed approximately toward an observer (the inclination angle of the observer is denoted $\theta_{\rm o}$). Clearly, $\gamma \gg 1$ implies that the scattered photons are boosted in the direction of motion. Although light bending increases the apparent size of the star on the particle local sky, general relativity effects are quite negligible on scattered photons moving straight away from the centre. Only few photons are scattered backwards, and therefore the direct image greatly dominates the signal received by an observer.

The measured radiation flux $S_{\rm tot}$ has two components: the primary unpolarized flux $S_\star$ and the flux of partially polarized radiation scattered in the cloud $S_{\rm cl}$. Their ratio can be given in terms of redshifted intensities $\tilde{I}_\star$ and $\tilde{I}_{\rm cl}$ of the star and of the cloud, and by the ratio of solid angles occupied by the cloud and by the star on the observer sky. This provides us with the estimation of the expected fractional polarization of the total signal. The ratio of fluxes is

$$s \equiv \frac{S_{\rm cl}}{S_\star} = \left(\frac{R_{\rm cl}}{R_\star}\right)^2 \frac{\tilde{I}_{\rm cl}}{\tilde{I}_\star}. \tag{41}$$

The intensity arriving from the cloud $\tilde{I}_{\rm cl} = \xi^2(r) I_{\rm sc}$, where $I_{\rm sc}(r)$ is the locally emitted intensity, as given by equation (17). The scattered component is polarized with the magnitude $\Pi_{\rm cl}$, as derived in the previous section. The total flux and the total polarization are

$$S_{\rm tot} = (1+s) S_\star, \qquad \Pi_{\rm tot} = \frac{s \Pi_{\rm cl}}{1+s}. \tag{42}$$

Substituting equation (17) into equation (42) we can verify that the flux ratio s does not depend on the star intensity $I_\star$, and hence

$$s = \kappa f(\beta, r, \vartheta), \tag{43}$$

where $\kappa \equiv \tau_{\rm cl}(R_{\rm cl}/R_\star)^2$ depends on the size and density of the cloud, and f includes the geometry of the radiation field and the beaming/aberration effects arising from the cloud motion. We consider situations when κ is small; then, the two contributions to the radiation intercepted by the observer become comparable only in the case of strong beaming, which leads to $f \gg 1$ for small observing angles.

The moment of observation, i.e. the arrival time of photons $t_{\rm obs}$ ($r \to \infty$), is related to the moment of emission t by

$$t_{\rm obs} \simeq t - \frac{1}{c}\,[z(t) - z_0] \cos\theta, \tag{44}$$

where we set $t(z_0) = 0$ for the initial time and $t_{\rm obs} = 0$ for the moment when the signal arrives at the observer. Notice that this estimate is sufficient for direct image photons discussed in this subsection, but it would not be appropriate for higher-order image photons in the next subsection (in Schwarzschild geometry, one can express time of arrival in terms of elliptic integrals, proceeding in the same analytical manner as above in the calculation of the ray trajectory; see also Bozza & Mancini 2004; Čadež & Kostić 2005).

The temporal behaviour is shown in Fig. 6. We assume that the cloud has been pre-accelerated to large initial speed $\beta(t = 0)$ near the star surface. The graph captures the subsequent phase of gravitational and radiative deceleration. The scattered light contributes

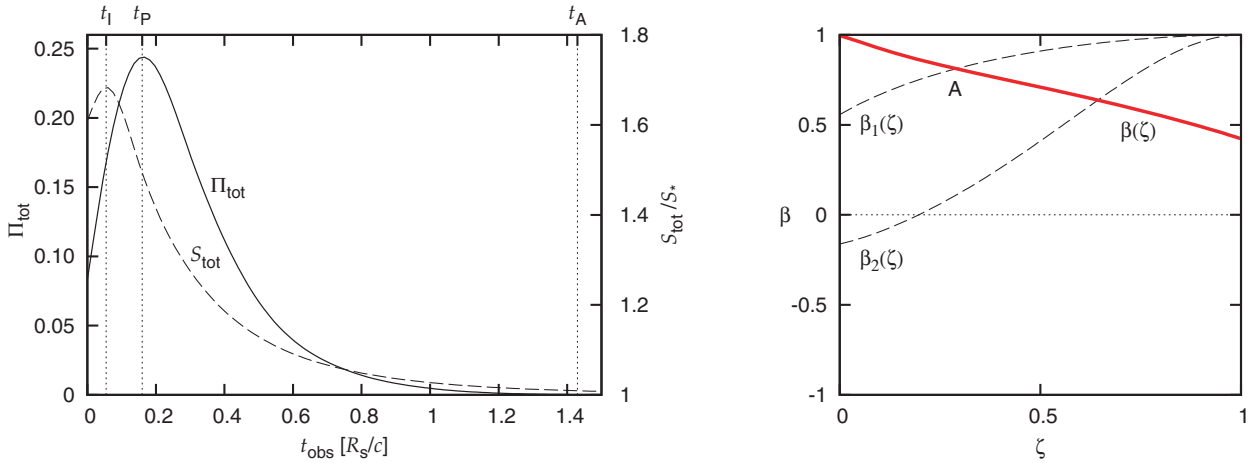

Figure 6. Left: the variation of the total normalized radiation flux $S_{\rm tot}(t)$ and the corresponding degree of polarization $\Pi_{\rm tot}(t)$. The case of ultrarelativistic ejection starting with initial $\gamma(R_\star) = 10$. Right: the corresponding velocity profile $\beta(\zeta)$ and critical velocities $\beta_{1,2}(\zeta)$ are shown. The parameters of the plot are $\theta = 17^\circ$, $R_\star = 1.2R_{\rm S}$. Polarization vanishes at point A when $\beta(\zeta) = \beta_1(\zeta)$; the corresponding time is $t = t_{\rm A}$ in the left panel. Polarization vanishes once again at a later time, when $\beta(\zeta) = \beta_2(\zeta)$.

significantly to the total signal only for a short initial phase (a peak occurs in the graph). The local maxima of the radiation flux (at $t = t_{\rm I}$) and of polarization (at $t = t_{\rm P}$) can be understood in terms of beaming: most of the radiation from the cloud is emitted in a cone with the opening angle $\sim 1/\gamma$ about the direction of motion. For small viewing angle ($\theta_{\rm o} \lesssim 13^\circ$) the observer was initially located outside this cone but, as time passes, the electron decelerates, the cone opens up and the observer intercepts more radiation. The maximum observed polarization occurs with a certain delay $t_{\rm P} - t_{\rm I}$ (proportional to M) after the peak of radiation flux. The subsequent decay of the signal is connected with a diminished scattering power of the cloud and the overall dilution of the radiation field. The observed polarization and the flux are lagged with each other and sensitive to the angle of observation. This behaviour is also clearly seen in Fig. 7, where we have assumed several different viewing angles.

We selected large initial velocity in this example, otherwise the effects of aberration and the Doppler boosting would be less prominent, time-scales longer, and the effect of the fractional polarization crossing zero-point would disappear. The time-span of this plot can be scaled according to the light-crossing time in physical units

$$t \simeq 1.5\frac{R_{\rm S}}{c} = 1.5\times 10^{-4}\frac{M}{10\,{\rm M}_\odot}\quad ({\rm s}), \tag{45}$$

i.e. proportionally to the central mass. The polarization magnitude is correlated with the intensity (this correlation was already noticed for the isotropic radiation in the right panel of Fig. 2).

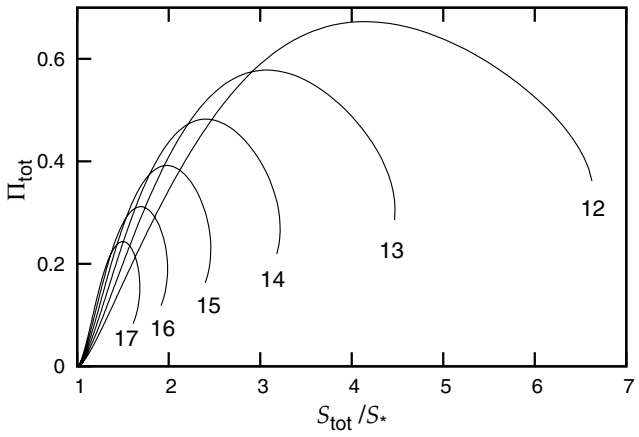

Figure 7. The relation between the normalized radiation flux and the total polarization. The magnitude of polarization $\Pi_{\rm tot}$ reaches up to $\sim$65 per cent for suitable view angles. Values of $\theta_{\rm o}$ (in degrees) are given with the curves. Other parameters are the same as in Fig. 6.

4.2 A cloudlet at rest ($\gamma = 1$)

An interplay between gravity and the ambient radiation stalls the bulk motion, $\beta(t) \to 0$. Scattered photons are then no longer boosted in the outward direction, and so the higher-order (highly bent) rays can provide a non-negligible contribution to the observed light after encircling the star. This of course requires large compactness; we set $R_\star = (3/2)R_{\rm S}$ hereafter. Again we assume an observer near the z-axis and a cloudlet with a small size, $\psi \ll 1$. Unlike a more traditional application of the lens geometry, the cloudlet is placed at an arbitrary finite distance, $z \equiv z(t)$, above the star and the deflection angle does not have to be small.

Let us consider rays making a single round (by the angle $\Theta = 2\pi \pm \theta_{\rm o}$), with a radial turning point at pericentre $r = r_{\rm p}$ tightly above the photon circular orbit. As mentioned in Section 3.3, the equilibrium radius depends on the star luminosity. Once the cloudlet settles at the equilibrium point $r = R_{\rm eq}$, scattered photons are no longer boosted to high energy and the collimation effect disappears. In this situation, relatively more light is backscattered in the direction toward the photon orbit. Some of these photons form a retrolensed image (Holz & Wheeler 2002), which may also reach the observer. We thus now calculate (de)magnification of light also for the two first-order images, which give the most significant contribution and may influence the net polarization at infinity. To this aim we need to consider rays starting near above the star, passing through pericentre and eventually escaping to infinity (the retrolensing geometry; see Ohanian 1987; Virbhadra & Ellis 2000; Bozza 2002, and references therein).

Two arcs are formed which merge together in the Einstein ring [with radius just above $b_{\rm c} = (3/2)\sqrt{3}\,R_{\rm S}$] if the observer is aligned

with the source. By integrating null geodesics, expanding the elliptic integrals near the pericentre $r_{\rm p} \sim (3/2)R_{\rm S}$, assuming the deflection angle close to $\Theta \sim 2\pi$, and keeping only the leading terms we obtain the desired width of the two retrolensing images

$$\delta b(\phi) = 2\,\delta b_0 \left(\psi^2 - \theta_{\rm o}^2 \sin^2\phi\right)^{1/2} \tag{46}$$

where $\delta b_0 = K(z)\,{\rm e}^{-2\pi}$, $|\phi| \leqslant \arcsin(\bar{\psi}/\theta_o)$, $\bar{\psi} = {\rm Min}\{\theta_o, \psi\}$, and

$$K = \frac{6^3\,3\sqrt{3}}{2}\,\frac{\sqrt{3}-1}{\sqrt{3}+1}\,\frac{\sqrt{3}-\sqrt{1+3u}}{\sqrt{3}+\sqrt{1+3u}}, \qquad u(z) \equiv \frac{R_{\rm S}}{z}. \tag{47}$$

We remark that $\Theta \sim 2\pi$ was assumed for simplicity only. The case of arbitrary Θ can be treated in a similar way.

The time dependence of the arcs is caused by the scatterer motion, $z = z(t)$. We integrate over the cross-section of the arc images to derive their total luminosity and polarization at each time moment. Higher-order images suffer from the demagnifying influence of the light bending, which reduces their luminosity, unless a special geometrical alignment of the source and the observer occurs and favours the opposite effect of a caustic. This can be quantified by the gain factor, $\mathcal{M}$, which determines the ratio of fluxes received in retrolensed/direct images. The problem translates to evaluating the ratio of solid angles, $\mathcal{M} \equiv {\rm d}\Omega_{\rm i}/{\rm d}\Omega_{\rm o}$, where indices 'i' and 'o' refer to the angular size of the source with and without taking the light bending into account. In the case of a small (but finite) size cloudlet, we find

$$\mathcal{M}(z) = 6\sqrt{3}\,K(z)\,{\rm e}^{-2\pi}\psi^{-1}\,\Lambda(\theta_{\rm o}/\psi), \tag{48}$$

where the term

$$\Lambda(k) \equiv \frac{2}{\pi}\,E(\Phi, k), \qquad \Phi \equiv \arcsin[{\rm Min}\{k^{-1}, 1\}], \tag{49}$$

arises from the integration over the Einstein arcs.

For $\psi \ll \theta_{\rm o}$ the gain function is

$$\mathcal{M}(z, \Theta) \simeq \frac{3}{2}\sqrt{3}\,K(z)\,\frac{R_{\rm S}^2}{z^2}\,\frac{\exp(-\Theta)}{|\sin\Theta|}. \tag{50}$$

Equation (51) reduces to equation (21) of Ohanian (1987) for $z \to \infty, \zeta(z) \to 1$. In our situation, equation (51) requires that the cloudlet is sufficiently small in size and its motion is directed somewhat sideways with respect to the observer view angle. Fig. 8 compares $\mathcal{M}(\zeta, \Theta)$ with the corresponding result of a numerical integration, showing that the approximation is sufficiently accurate for our purposes.

Adding the contributions from different parts of the source has a depolarizing effect on the final signal, which we illustrate in Fig. 9. For the total magnitude of polarization of the retrolensing images we find

$$\Pi_{\rm ret} = \Pi(\vartheta_{\rm ph})\,p(\theta_{\rm o}/\psi), \tag{51}$$

where $\Pi(\vartheta_{\rm ph})$ is the polarization magnitude of light scattered in the direction towards the photon circular orbit and

$$p(k) \equiv \frac{2}{\pi\Lambda(k)}\int_0^{\Phi} \cos 2\phi\,\sqrt{1-k^2\sin^2\phi}\;{\rm d}\phi. \tag{52}$$

Functions Λ and Φ were defined in equation (50). Function p determines the shape of retrolensing images in the observer plane; see Fig. 10 (we resolve a narrow trace of these arcs on the observer sky by enlarging their separation $\delta b \equiv b - b_{\rm c}$ from the critical radius $b_{\rm c}$). The polarization vectors of all three images have the same orientation, but they experience different time delays and lensing along each trajectory. The contribution of the retrolensed images is now evident, and quite significant. Notice that the angle $\vartheta_{\rm ph}$ is the apparent angular size of the photon orbit as seen on the local sky of the cloudlet. It enters in equation (52) because higher-order images are formed almost exclusively by light scattered on the photon circular orbit. In our case, $\vartheta_{\rm ph} = \alpha_\star(z)$. The polarization magnitude drops sharply if the observer inclination is less than the angular size of the cloudlet.

4.3 Comparison between an outflow and an inflow

Now we consider an intermediate situation with moderate velocity of the bulk motion (both an outflow or an inflow, i.e. $\beta >rless 0$). For a moderate outflow velocity, the result is shown in Fig. 11. We consider a particle on the decelerating branch of the trajectory in a weak radiation field, $\Gamma \to 0$, which eventually reaches the turning point (and starts falling afterwards). The two retrolensed images contribute about 10 per cent of the scattered flux at maximum and the trajectory crosses the $\beta = \beta_2(\xi)$ curve, where the polarization vector swings its direction. The outcome is quite different for matter infalling on to the star, because scattered photons are boosted in the downward direction and a considerable amount of light is then

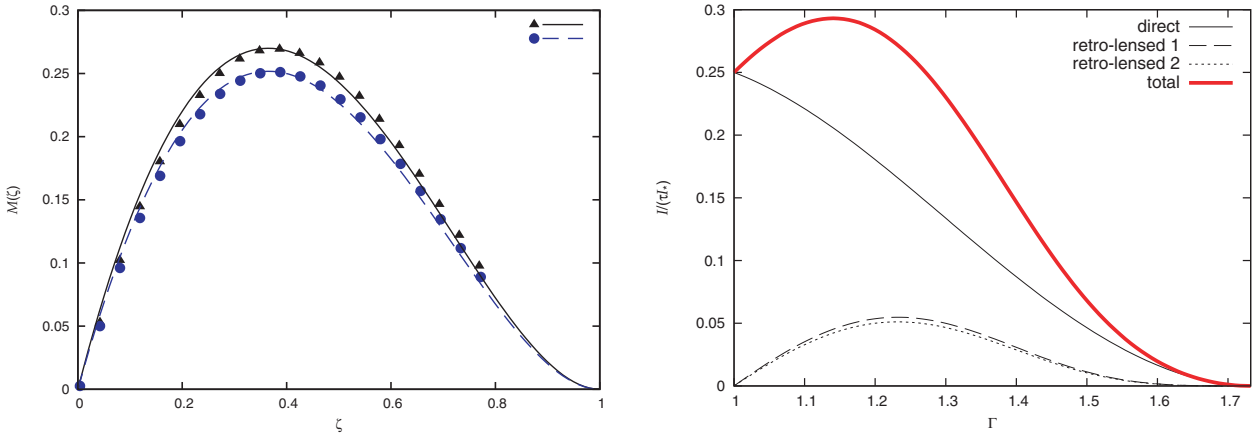

Figure 8. Left: the gain factor $\mathcal{M}(\Theta, \zeta)$ according to the approximation equation (51). Two curves are shown as a function of the source distance ζ, for $\Theta = 358^\circ$ (solid line) and $\Theta = 362^\circ$ (dashed line). For comparison, exact (numerically computed) values are also plotted with triangles and circles. Right: normalized intensity of the direct image (thin solid line) and the two retrolensed images (dashed and dotted lines) of light scattered from a particle residing in the equilibrium point $z = R_{\rm eq}$, as a function of the Eddington parameter. Notice that the contribution of the two retrolensed images is almost identical and it amounts up to ~20 per cent of the total signal (thick solid line). Inclination $\theta_{\rm o} = 2^\circ$ in both panels.

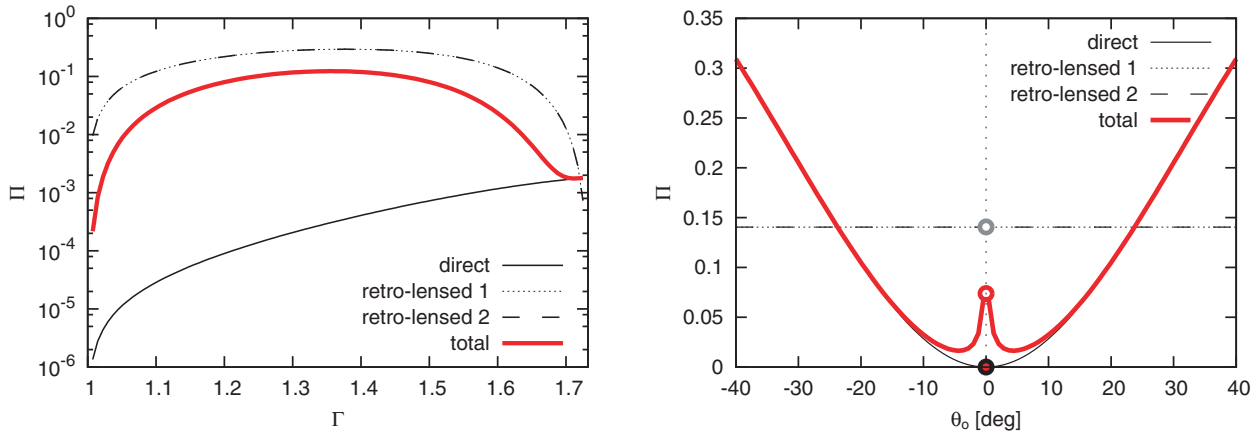

Figure 9. Polarization magnitude from scattering on a particle at rest at $z = R_{\rm eq}$. This represents a cloudlet of angular radius ψ on the local sky of the star. Left: the observed polarization magnitude as a function of Eddington parameter Γ. Notice that $R_{\rm eq}$ is a function of Γ, and so the graph covers the whole range of radii from the star surface to infinity. The observer inclination is $\theta_{\rm o} = 2^\circ$. Right: the corresponding polarization magnitude for different inclinations and constant $\Gamma = 1.6$ (in the case of precise alignment, $\theta_{\rm o} = 0^\circ$, polarization vanishes because of symmetry).

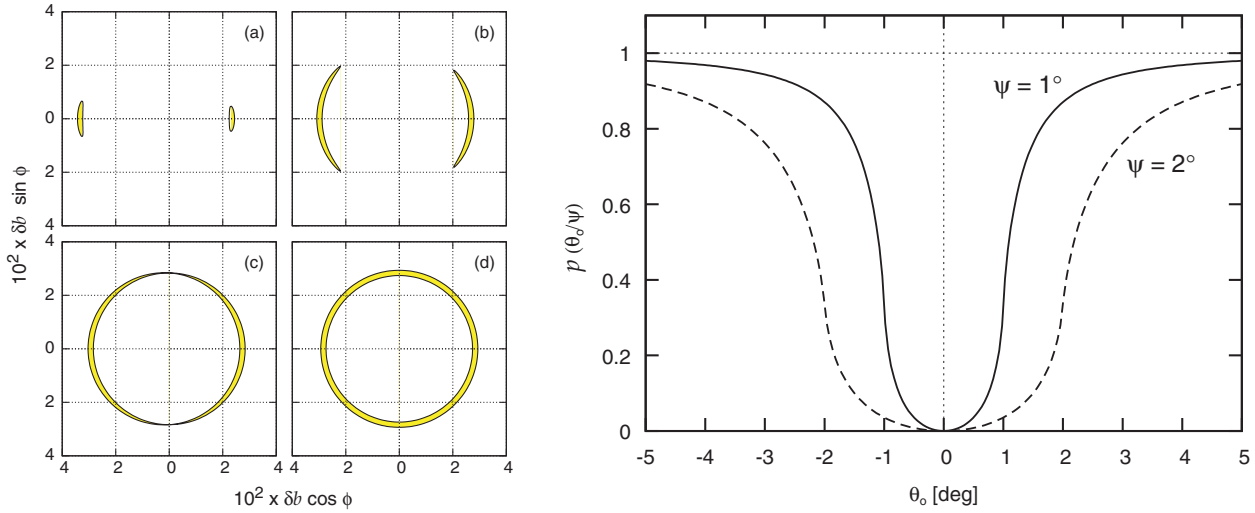

Figure 10. Left: the form of Einstein arcs (a)–(c) and the ring (d) corresponding to the retrolensing images in polar coordinates (b, ϕ) in the observer plane. The source is supposed to be a circular target of angular radius $\psi = 2^\circ$, located on the z-axis at distance $z = 3R_{\rm S}$. The observer is at $r \to \infty$ and has a small angular offset from the perfect alignment: (a) $\theta_{\rm o} = 10^\circ$; (b) $\theta_{\rm o} = 2^\circ$; (c) $\theta_{\rm o} = 1^\circ$; (d) $\theta_{\rm o} = 0^\circ$. Right: a contribution to the polarization produced by the Einstein arcs. A detail of the normalized magnitude p is plotted for small values of inclination; see equation (52) for the definition of function $p(\theta_{\rm o}/\psi)$. For large $\theta_{\rm o}$ the magnitude of polarization saturates at roughly constant level, equal to the polarization scattered in the direction toward the photon circular orbit. The two curves are parametrized by the angular size ψ of the cloudlet, as indicated in the plot.

directed on to the photon orbit. As a result, the retrolensed images are more pronounced and they cause a brief flash of light. The resulting signal is shown in Fig. 12.

The effect of retrolensed images is clearly visible in the polarization curve (see Fig. 13). The case shown in the left panel exhibits a brief drop of the polarization magnitude when velocity crosses $\beta = \beta_2(\zeta)$ (the direct image arrives at $t \sim 1$ in dimensionless units). At this moment the polarization changes its orientation between transversal and longitudinal polarization. Then the signal is restored back to a non-zero value and the same behaviour repeats when the retrolensed image arrives after a certain delay (at $t \sim 21$). The case shown in the right panel exhibits a similar flash, also caused by the contribution of the retrolensed photons. However, now we observe a single fluctuation, which is actually an increase of the polarization magnitude; this is because the case shown here corresponds to transversal polarization during the whole observation and the trajectory does not cross any of the critical curves $\beta = \beta_{1,2}$.

5 CONCLUSIONS

Our calculation here is self-consistent in the sense that the motion of the blob and of photons, and the resulting polarization are mutually connected. We have concentrated on gravitational effects and neglected other intervening processes, first of all the effect of magnetic fields to which polarization is sensitive (see, for example, Agol & Blaes 1996). This allowed us to compare polarization magnitudes of direct and retrolensed images, which could point to the presence of a highly compact body. We have noticed the mutual delay between the signal formed by photons of different order. The delay is characteristic of the effect and has a value proportional to the central mass.

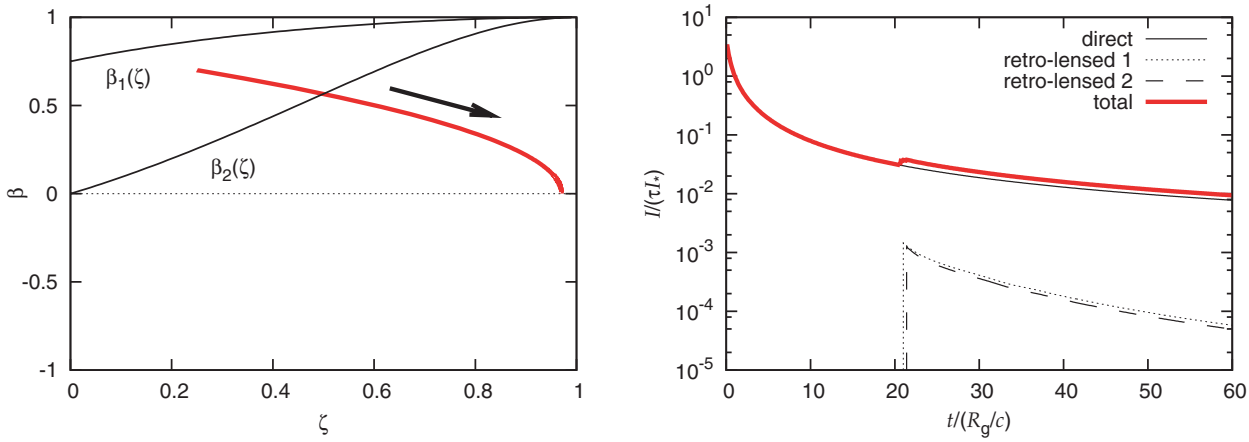

Figure 11. An outward-moving particle decelerating in the gravitational and weak radiation fields. Left: the trajectory in the (β, ζ)-plane, i.e. dimensionless velocity versus distance (thick solid line). Velocity changes in the direction of the arrow. Right: the radiation flux of scattered light as a function of time for the direct and two retrolensed images. The initial condition is $\beta = 0.7$ at $r = 2R_S$. The observer inclination is $\theta_o = 5^\circ$.

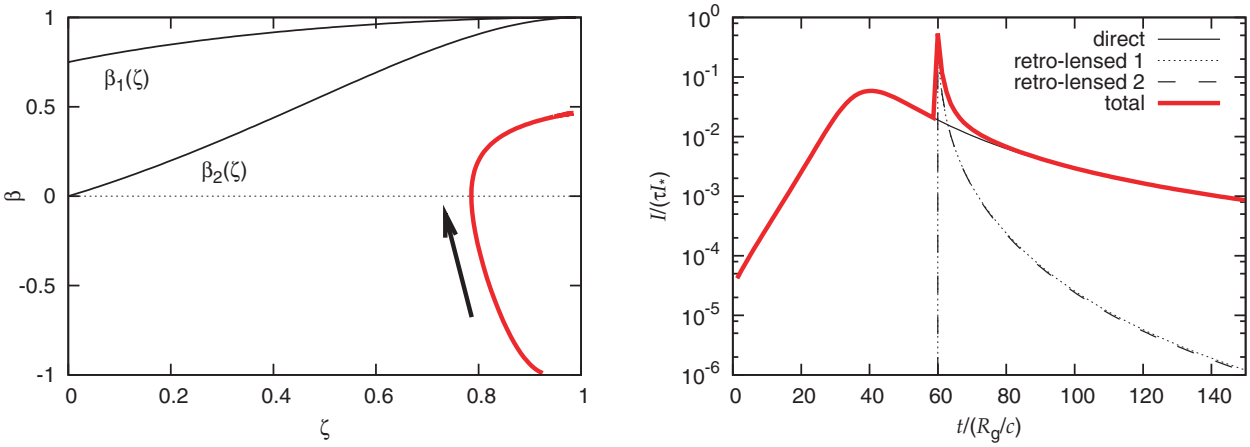

Figure 12. The same as in Fig. 11, but for fast inward motion of the scatterer and strong radiation of the star ($\Gamma = 10$). We set $\beta = -0.99$, $r = 20R_S$ as an initial condition at $t = 0$. The signal of the higher-order image flashes for a brief moment around dimensionless time $t \simeq 60$. The intense radiation of the star reverses the particle velocity to the outward motion at later stages. The observer inclination is $\theta_o = 2^\circ$.

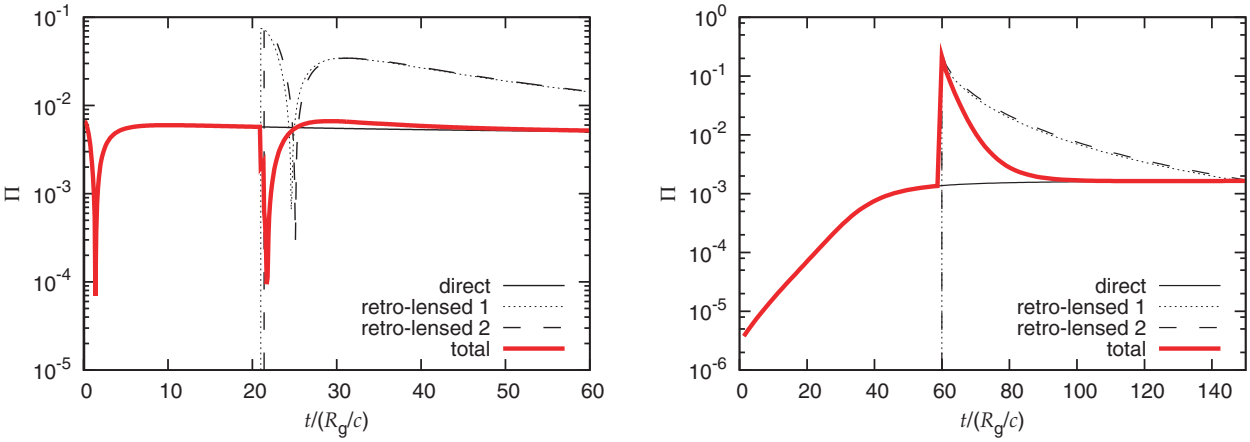

Figure 13. The magnitude of polarization corresponding to the case shown in Fig. 11 (left panel) and in Fig. 12 (right panel). The retrolensed signals are delayed with respect to the direct signal. The delay has a value characteristic to light traveltime along the photon circular orbit (it scales proportionally to the mass of the central body). The total polarization is suppressed or enhanced depending on the mutual relation between the polarization of direct and retrolensed photons.

Polarimetric properties are susceptible to large changes depending on detailed physics and geometry of the source, and this is not only an advantage, which could help us to trace how different objects are functioning, but also a complication. In particular, the polarization is sensitive to the source orientation and its magnitude fluctuates from case to case. Our results are useful for testing more complex and astrophysically realistic models with upscattering of soft photons in jets and fast flows around black holes. In the black hole case, the primary photons would be provided by an accretion disc rather than the star surface and, hence, we can no longer take advantage of its spherical symmetry, which helped us to simplify our calculations here. None the less, the same formalism can be employed and similar features of time-dependent polarization light curves are expected; strong gravity plays a vital role again. Putting this in another way, provided a 'realistic' equation of state implies neutron star radii greater than the photon circular orbit, the detection of the signatures of retrolensing images, which we have discussed above, would exclude a neutron star as a candidate on the central body.

ACKNOWLEDGMENTS

The authors thank John Miller for his advice on the current status of neutron star modelling, and an anonymous referee for critical comments on the first version of the paper. VK appreciates fruitful discussions with participants of the Aspen Center for Physics 2005 Workshop on Revealing Black Holes. The financial support for this research has been provided by the Academy of Sciences (grant IAA 300030510) and by the Czech Science Foundation (grant 205/03/0902). The Astronomical Institute has been operated under the project AV0Z10030501.

REFERENCES

Abramowicz M. A., Ellis G. F. R., Lanza A., 1990, ApJ, 361, 470
Agol E., Blaes O., 1996, MNRAS, 282, 965
Alcock C., Farhi E., Olinto A., 1986, ApJ, 310, 261
Angel J. R. P., 1969, MNRAS, 158, 219
Bao G., Hadrava P., Wiita P. J., Xiong Y., 1997, ApJ, 487, 142
Begelman M. C., Sikora M., 1987, ApJ, 322, 650
Beloborodov A. M., 1998, ApJ, 496, L105
Bonometto S., Cazzola P., Saggion A., 1970, A&A, 7, 292
Born M., Wolf E., 1964, Principles of Optics. Pergamon Press, Oxford
Bower G. C., Falcke H., Wright M. C. H., Backer D. C., 2005, ApJ, 618, L29
Bozza V., 2002, Phys. Rev. D, 66, 103001
Bozza V., Mancini L., 2004, Gen. Rel. Grav., 36, 435
Brown J. C., McLean I. S., 1977, A&A, 57, 141
Brown E. F., Bildsten L., Rutlege R. E., 1998, ApJ, 504, L95
Čadež A., Kostić U., 2005, preprint (gr-qc/0405037)
Celotti A., Matt G., 1994, MNRAS, 268, 451
Chandrasekhar S., 1960, Radiative Transfer. Dover, New York
Chandrasekhar S., 1992, The Mathematical Theory of Black Holes. Oxford Univ. Press, New York
Chandrasekhar S., Ferrari V., 1991, Proc. R. Soc. London A, 434, 449
Cocke W. J., Holm D. A., 1972, Nat, 240, 161
Combi J. A., Cellone S. A., Martí J., Ribó M., Mirabel I. F., Casares J., 2004, A&A, 427, 959
Connors P. A., Stark R. F., Piran T., 1980, ApJ, 235, 224
Dey M., Bombaci I., Dey J., Ray S., Samanta B. C., 1998, Phys. Lett. B, 438, 123
Fox G. K., 1994, ApJ, 435, 372
Fukue J., Hachiya M., 1999, PASJ, 51, 185
Ghisellini G., Lazzati D., 1999, MNRAS, 309, L7
Ghisellini G., Haardt F., Matt G., 2004, A&A, 413, 535
Haensel P., 2003, in Motch C., Hameury J.-M., eds, Final Stages of Stellar Evolution. EAS Publications Series, EDP Sciences, p. 249
Haensel P., Zdunik J. L., 1990, A&A, 227, 431
Holz D. E., Wheeler J. A., 2002, ApJ, 578, 330
Horák J., 2005, PhD Thesis, Charles Univ. Prague
Keane A. J., Barrett R. K., Simmons J. F. L., 2001, MNRAS, 321, 661
Kokkotas K. D., Ruoff J., Andersson N., 2004, Phys. Rev. D, 70, 043003
Lattimer J. M., Prakash M., 2001, ApJ, 550, 426
Lattimer J. M., Prakash M., 2004, Sci, 304, 536
Lazzati D., Rossi E., Ghisellini G., Rees M. J., 2004, MNRAS, 347, L1
Levinson A., Eichler D., 2004, ApJ, 613, 1079
Lightman A. P., Shapiro S. L., 1975, ApJ, 198, L73
McClintock J. E., Narayan R., Rybicki G. B., 2004, ApJ, 615, 402
Mazur E., Mottola P. O., 2004, Proc. Nat. Acad. Sci., 111, 9545 (gr-qc/0109035)
Melia F., Königl A., 1989, ApJ, 340, 162
Miller J. C., Shahbaz T., Nolan L. A., 1998, MNRAS, 294, L25
Ohanian H. C., 1987, Am. J. Phys., 55, 428
Pineault S., 1977, MNRAS, 179, 691
Poeckert R., Marlborough J. M., 1976, ApJ, 206, 182
Portsmouth J., Bertschinger E., 2005, preprint (astro-ph/0412094)
Poutanen J., 1994, ApJS, 92, 607
Rees M. J., 1975, MNRAS, 171, 457
Rudy R. J., 1978, PASP, 90, 688
Rybicki G. B., Lightman A. P., 1979, Radiative Processes in Astrophysics. Wiley, New York
Scaltriti F., Bodo G., Ghisellini G., Gliozzi M., Trussoni E., 1997, A&A, 325, L29
Shaviv N. J., Dar A., 1995, ApJ, 447, 863
Sikora M., Wilson D. B., 1981, MNRAS, 198, 529
Sunyaev R. A., Titarchuk L. G., 1985, A&A, 143, 374
Synge J. L., 1967, MNRAS, 136, 195
Viironen K., Poutanen J., 2004, A&A, 426, 985
Virbhadra K. S., Ellis G. F. R., 2000, Phys. Rev. D, 62, 084003
Vokrouhlický D., Karas V., 1991, A&A, 252, 835
Weber F., 2005, Prog. Part. Nucl. Phys., 54, 193
Winterberg F., Phillips W. G., 1973, Phys. Rev. D, 8, 3329

This paper has been typeset from a TEX/LATEX file prepared by the author.